Research Article Vol. 8, No. 12 / December 2021 / Optica 1545

Ultra-thin plasmonic detectors

Leland Nordin, Priyanka Petluru, Abhilasha Kamboj, Aaron J. Muhowski, and Daniel Wasserman*

Department of Electrical and Computer Engineering, University of Texas at Austin, Austin, Texas 78758, USA
**Corresponding author: dw@utexas.edu*

Received 16 July 2021; revised 31 October 2021; accepted 1 November 2021; published 8 December 2021

Plasmonic materials, and their ability to enable strong concentration of optical fields, have offered a tantalizing foundation for the demonstration of sub-diffraction-limit photonic devices. However, practical and scalable plasmonic optoelectronics for real world applications remain elusive. In this work, we present an infrared photodetector leveraging a device architecture consisting of a "designer" epitaxial plasmonic metal integrated with a quantum-engineered detector structure, all in a mature III-V semiconductor material system. Incident light is coupled into surface plasmon-polariton modes at the detector/designer metal interface, and the strong confinement of these modes allows for a sub-diffractive ($\sim\lambda_0/33$) detector absorber layer thickness, effectively decoupling the detector's absorption efficiency and dark current. We demonstrate high-performance detectors operating at non-cryogenic temperatures ($T = 195$ K), without sacrificing external quantum efficiency, and superior to well-established and commercially available detectors. This work provides a practical and scalable plasmonic optoelectronic device architecture with real world mid-infrared applications.

https://doi.org/10.1364/OPTICA.438039

1. INTRODUCTION

The field of nanophotonics has been driven by the desire to demonstrate optical structures capable of sub-diffractive confinement of light, and to subsequently leverage these structures to develop optoelectronic devices capable of emitting, detecting, and/or manipulating light at these same sub-diffractive length scales. The field of plasmonics has long been central to such efforts, as the strong optical confinement provided by plasmonic structures offers a path towards sub-diffraction-limit optical waveguides, sources, and sensors [1–9]. However, while plasmonic devices can offer impressive mode confinement, they often underperform diffraction-limited devices on most other metrics [10]. The prospects for scalable plasmonic architectures for real world applications have thus largely been limited, and plasmonics has had its greatest impact in applications where the strong optical mode confinement benefits all-optical sensing of small material volumes [11,12] or localized heat generation [13,14], neither of which is a true optoelectronic realization of plasmonic enhancement. Transitioning plasmonics from optical structures [15] to optoelectronic devices [16] has not, until now, resulted in performance competitive with existing diffraction-limited technologies.

For the longer wavelengths of the mid-infrared (mid-IR, 3−20 μm) and particularly in the long-wave IR (LWIR, 8−13 μm), achieving nano-scale devices is substantially more challenging than at shorter wavelengths where the bulk of plasmonics research efforts are undertaken [17]. This is partially a result of the order of magnitude increase in wavelength (and proportionally, the diffraction limit) as one moves from the near-IR/visible (near-IR/vis) wavelength range to the LWIR, but also because the traditional plasmonic metals of the near-IR/vis, with increasing wavelength, behave more and more like perfect electrical conductors, and are unable to support highly confined plasmonic modes [18]. However, in the mid-IR, highly doped semiconductors (often referred to as "designer" metals), can be used as plasmonic materials [19,20]. High-quality, single-crystal IR plasmonic doped semiconductors can be grown by molecular beam epitaxy (MBE), with the exquisite control of layer thickness and free carrier concentration afforded by epitaxial growth.

Importantly, doped semiconductor plasmonic materials can be seamlessly integrated with MBE-grown quantum-engineered optoelectronic active regions [21,22]. Notably, the class of semiconductor heterostructures known as type-II superlattices (T2SLs), consisting of alternating layers of III-V semiconductor alloys with type-II band offsets, allows for engineering of effective bandgap energies across the IR, including energies well below the bandgap of the superlattice's constituent materials [Fig. 1(c)]. T2SLs are of particular interest for IR detectors, due to suppressed Auger recombination [23], and have been integrated into a variety of IR detector architectures. In particular, LWIR T2SLs have been used in so-called "bariode" devices such as the nBn detector, which consists of an n-doped absorber (n), a wide bandgap barrier (B) and a thin, n-doped contact layer (n). Photocurrent is carried by photo-excited holes (minority carriers), while the wide bandgap barrier blocks transport of the majority carrier electrons, substantially reducing dark current and dramatically improving detector performance [24,25]. The ability to directly integrate these quantum-engineered IR active devices with plasmonic materials, in an all-epitaxial system, provides a complete materials framework

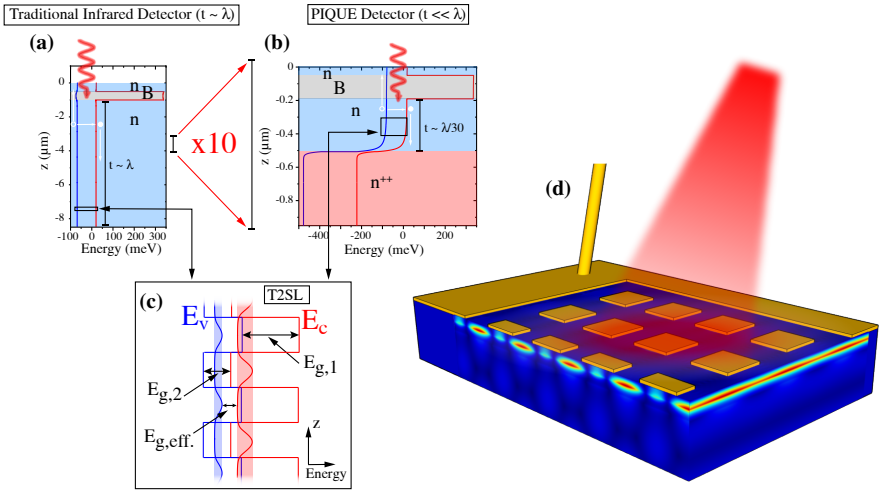

Fig. 1. Depiction of the relative length scale of (a) traditional LWIR detector architecture compared to (b) our plasmonic infrared quantum-engineered ultra-thin epitaxial (PIQUE) detector. Both (a) and (b) show the detector effective band structure, while (c) shows the band structure of the quantum-engineered type-II superlattice absorbers. (d) Isometric schematic of the PIQUE detector with overlaid $|Hy|^{TM}$ field profiles at the resonant frequency of the PIQUE detector ($\lambda = 10.7$ μm). A significantly enhanced field amplitude is present in the PIQUE detector, due to the plasmonic mode, resulting in strong absorption in the ultra-subwavelength thickness ($\ll \lambda_0$) absorber region. State-of-the-art performance is enabled by integrating the quantum-engineered type-II superlattice absorbers in an nBn detector architecture to overlap with the strongly confined SPP mode at the interface between the n^{++} semiconductor and the detector stack.

for the design of scalable sub-diffraction-limit detectors, or more generally, optoelectronic devices, in a wavelength range of vital importance for a host of sensing and imaging applications.

To quantify the benefits associated with sub-diffraction-limit thickness detector architectures, we consider the figure of merit specific detectivity (D^*), used to evaluate IR photodetector performance across detector architectures. Assuming uniform thermal generation and recombination rates, specific detectivity can be expressed as [26]

$$D^* = \frac{\lambda_0 \eta}{hc\sqrt{2t(G+R)}} \frac{A_o}{A_e}, \tag{1}$$

where λ_0 is the wavelength of light, η is the external quantum efficiency (EQE) of the detector (defined as the ratio of collected charge carriers to incident photons), h is Planck's constant, c is the speed of light, t is the detector absorber thickness, G and R are the absorber generation and recombination rates, respectively, and A_o and A_e are the device optical and electrical areas, respectively. Optimizing detector performance, for a given wavelength and lateral geometry (A_o and A_e), requires maximizing $\eta/\sqrt{t(G+R)}$: achieving high quantum efficiency while minimizing absorber thickness or the generation and/or recombination rates of carriers. Mercury cadmium telluride (MCT) has been the material system of choice for IR detectors for the last 60 years, due to its high quantum efficiency and small generation and recombination rates. Recent results [27] have shown that careful heterostructure engineering can further reduce the generation and recombination rates of MCT detectors and therefore substantially lower their dark current. Although these results are encouraging, there is still interest in supplanting MCT due to environmental concerns associated with Hg and Cd [28]. III-V semiconductor-based detectors have been identified as a candidate replacement for MCT, as these detectors benefit from more uniform growth, widely used commercial substrates, and substantially easier fabrication [29]. However, some of the most promising III-V-semiconductor-based detector candidates, quantum dot or quantum well IR photodetectors (QDIPs and QWIPs, respectively), have struggled to realize EQE within an order of magnitude of MCT detector EQE [30–32]. T2SL detectors on the other hand have struggled to achieve dark currents less than an order of magnitude above the longstanding MCT heuristic for dark current, Rule 07 [33]. In either case, the sub-optimal EQE or alternatively, dark current, ensures, for III-V-semiconductor-based detectors, D^*'s well below those of MCT. To compete with existing MCT technology, next-generation IR detectors must be able to minimize detector thickness, or reduce generation/recombination rates, while maintaining the EQE typical of existing, wavelength-scale-thickness detectors and do so in an environmentally manageable material system. To this end, leveraging plasmonic modes for strong light confinement in detector absorbing regions allows for the decoupling of detector thickness and absorption efficiency, and provides a path towards high quantum efficiencies in ultra-thin absorbers, and therefore superior D^*.

In this work, we design, grow, fabricate, and characterize monolithically integrated and sub-diffraction-limit-thickness LWIR detectors leveraging surface plasmon-polaritons (SPPs) at an epitaxial quantum-engineered absorber/designer metal interface. We dub these devices plasmonic IR quantum-engineered ultra-thin epitaxial (PIQUE) detectors, and show that the PIQUE device architecture can dramatically reduce deleterious detector properties such as dark current, resulting in low-noise operation while maintaining state-of-the-art detector response, all in a mature III-V semiconductor material system. The temperature-dependent electrical and optical properties of fabricated detectors are characterized experimentally, and the optical response is compared to rigorous coupled wave analysis and finite element method simulations with excellent agreement. The PIQUE detectors presented outperform state-of-the-art commercial detectors, both MCT and T2SL detectors [34,35], operate at temperatures compatible with thermo-electric coolers (TECs), and have the potential to extend efficient LWIR detector operation to room temperatures.

By monolithically integrating semiconductor plasmonic materials with sub-diffraction-limit-thickness optoelectronic active regions, this work demonstrates, for the first time, a scalable plasmonic optoelectronic architecture leveraging epitaxial plasmonic materials, and, importantly, a new approach to the design and development of mid-IR optoelectronic devices.

2. RESULTS

A. Device Design

Figure 2 shows the layer stack, simulated absorption, and on-resonance field contour plots ($|H_y|^{TM}$) for a variety of ultra-thin detector designs. In each simulation, the same nBn detector structure is used (311 nm absorber, 146 nm barrier, and 46 nm contact layer), and we plot the total simulated absorption (black), as well as the absorption in each of the layers: the detector absorber layer (red), contact layer (green), patterned grating layer (gold), and n^{++} ground-plane (blue). In Fig. 2(a), we show the absorption from a "bare" ultra-thin detector, grown on a lossless high-index substrate (GaSb), for which minimal LWIR absorption is observed. Adding metallic (Au) gratings to the bare detector [Fig. 2(b)] does little to enhance absorption, suggesting that such metal gratings do not act as resonant antennas, and are not responsible for any significant absorption enhancement. However, replacing the high-index, lossless substrate of the bare detector with a plasmonic (highly doped n^{++}) semiconductor does result in a significant absorption enhancement. This absorption is associated with a leaky mode of the air–detector–n^{++} stack, and has been demonstrated, and leveraged, for enhanced detection (or emission), using all-epitaxial plasmonic materials [21,22]. However, though such structures include "plasmonic" materials, they cannot be considered plasmonic devices, as they do not leverage plasmonic modes (and the associated strong confinement achievable with such modes), as evidenced by the field plot in Fig. 2(c). Additionally, the leaky mode absorption observed in Fig. 2(c) requires an air or other low-index superstrate above the detector, making this architecture unrealistic for future substrate-side-illumination detector designs.

Adding a grating structure to the detector with the n^{++} ground-plane results in a significant additional enhancement of absorption. We show simulation results for gratings (width 1.5 μm and period 3 μm) consisting of a high-index, lossless dielectric [Fig. 2(d)], the same n^{++} semiconductor of the heavily doped ground-plane [Fig. 2(e)], and Au [Fig. 2(f)]. All three simulated devices show similar mode profiles on resonance. In addition, all three simulated devices show a strong increase in absorption compared to the planar structure of Fig. 2(c) The interface modes of Figs. 2(d)–2(f) are identified as SPP modes, clearly bound to, and with peak intensity at, the absorber/n^{++} interface. Below the interface, the SPP decays rapidly in the plasmonic n^{++} layer. Above the interface, the SPP mode decays into the (dielectric) detector stack such that the upper half of the mode is almost entirely confined in the ultra-thin ($t = 311$ nm) absorber layer. The majority of the total absorption is shared between the absorber layer and the plasmonic n^{++} ground-plane, as would be expected for an SPP mode bound to this interface. While the patterned 2D grating on the detector surface provides in-plane momentum for coupling into the SPP modes, the strong mode confinement (and thus overlap of the optical field with the detector absorber) comes from the plasmonic mode supported by the n^{++} ground-plane.

The 2D metal grating [Fig. 2(f)] can be replaced with patterned highly doped plasmonic [Fig. 2(e)] or undoped dielectric

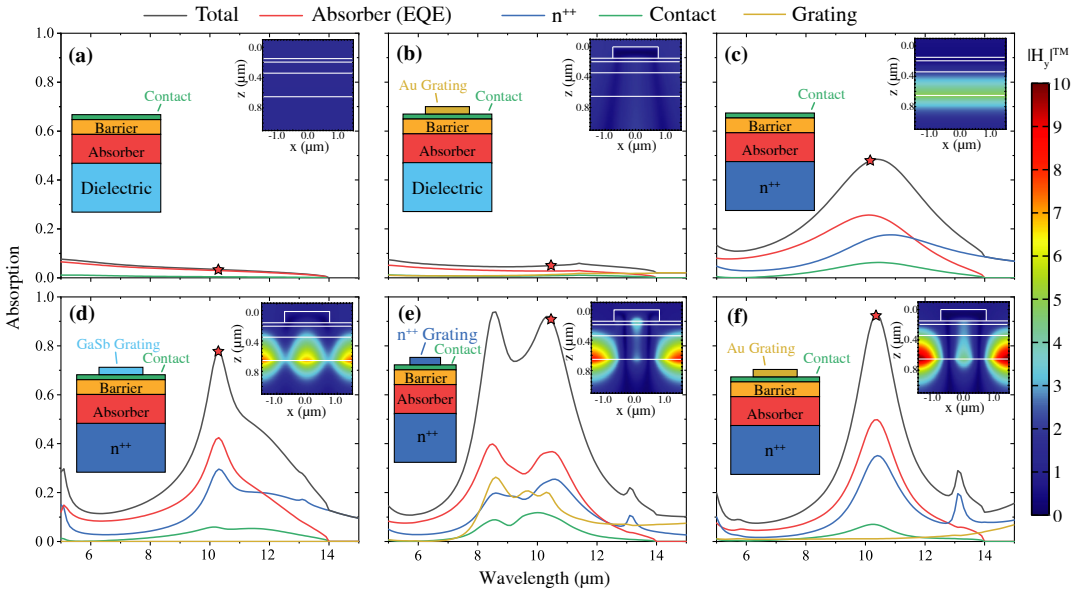

Fig. 2. Simulated absorption for six candidate ultra-thin detector architectures: (a) ultra-thin *nBn* detector grown above a high-index dielectric ground-plane with no surface patterning; (b) *nBn* detector grown above a high-index dielectric ground-plane patterned with a Au grating coupler; (c) *nBn* detector grown above a n^{++} ground-plane with no surface patterning; (d) *nBn* detector grown above a n^{++} ground-plane and patterned with a dielectric (GaSb) grating coupler; (e) *nBn* detector grown above a n^{++} ground-plane and patterned with a n^{++} grating coupler; (f) nBn detector grown above a n^{++} ground-plane and patterned with a Au grating coupler. For each configuration, we plot the total simulated absorption (black), as well as the absorption in each of the layers: the detector absorber layer (red), contact layer (green), grating (gold), and n^{++} ground-plane (blue). Provided in the inset of each plot is the $|H_y|^{TM}$ field contour at the wavelength indicated by a red star on the total absorption curve. While (c)–(f) all show resonant behavior, only (d)–(f) show coupling to a surface plasmon-polariton, which requires both the momentum imparted by the grating and the n^{++}/absorber interface necessary to support the plasmonic mode.

[Fig. 2(d)] semiconductor material with minimal effect on the detector's optical properties (or the optical mode excited). We do note an additional absorption feature for the n^{++} grating that we associate with coupling to the SPP via the localized surface plasmon resonance of the subwavelength n^{++} grating feature (such detector designs are the focus of future research efforts). It is thus clear that the metal layer serves only as a grating to couple light in to the SPP mode supported by the n^{++} ground-plane, and not as an antenna. Notably, the metallic grating coupler has negligibly low absorption [<1%, from Fig. 2(f)], further confirming that the mode is primarily bound to the epitaxial n^{++}/detector interface, not the metallic grating coupler. Moreover, if the n^{++} layer were to be replaced by a traditional high-index, and lightly doped substrate, as shown in Fig. 2(b), all enhancement is lost. These two effects underscore that the plasmonic nature of the device comes from the doped semiconductor ground-plane, and not the metallic grating. The PIQUE detectors presented in this work leverage the device design of Fig. 2(f), not only because this design shows the highest peak response, but also because the metal gratings can be patterned and deposited at the same time as the device contacts, simplifying device fabrication.

B. Optical Properties and External Quantum Efficiency

The PIQUE detectors are grown by MBE on GaSb substrates, and consist of a T2SL nBn detector with absorber/barrier/contact thicknesses of 311/146/46 nm above an epitaxially grown n^{++} semiconductor designer metal. Figure 1(b) shows the growth stack and simulated band structure for the PIQUE detector. The 2D metal grating (width 1.5 μm and period 3 μm) is patterned on the detector surface [as shown schematically in Figs. 1(d)] to enable polarization-independent coupling into the SPP modes supported at the absorber/n^{++} interface. Detector dimensions (n^{++}, contact, barrier, absorber layer thicknesses, grating period, and duty cycle) were optimized to give ultra-thin detectors (thus resulting in low dark currents), which could still achieve the integrated absorption/EQE (in the 8–13 μm LWIR) of traditional, wavelength-scale thickness T2SL detectors [36–38]. Epitaxial growth, detector fabrication, material and device characterization, and material optical properties are described in further detail in Supplement 1.

The experimental room temperature reflection spectrum of a fabricated detector is shown in Fig. 3(a), where the prominent dip in reflection at $\lambda_0 = 10.7$ μm corresponds to coupling into SPP modes, as can be seen from the simulated field profile of the structure shown in Fig. 2(f). In the LWIR, there is little transmission through the n^{++} ground-plane and no diffraction from the $\Lambda = 3$ μm grating; thus, reflection (R) in the LWIR can be related to total absorption (A) by the simple relation $A \simeq 1 - R$. While a significant amount of this absorption occurs in the detector absorber (where it will be converted to photocurrent), some fraction will also be absorbed by the n^{++} ground-plane and (to a much lesser extent) the gratings (light that will not be converted to photocurrent). While such loss is inevitable in strongly confined plasmonic modes, the total absorption in the detector absorber region remains comparable to the absorption of traditional wavelength-scale-thickness LWIR T2SLs [36–38].

The resulting spectral EQE for a detector with 2D metal grating element width 1.5 μm and period 3 μm is shown in Fig. 3(b) and compared to finite element simulations of EQE for the same device with (red dashed) and without (blue dashed) n^{++} ground-plane and 2D grating. Strong response is observed across the LWIR,

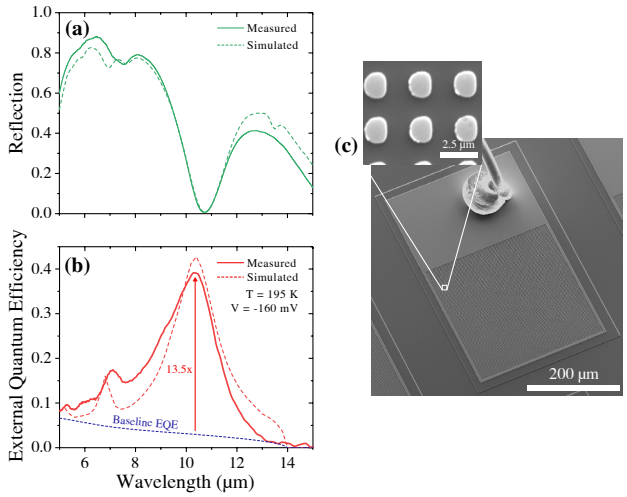

Fig. 3. (a) Experimental (solid) and RCWA-simulated (dashed) room-temperature reflection spectra from the fabricated detector structure (b) External quantum efficiency of the PIQUE detector operating at 195 K with a low reverse bias of −160 mV. The red solid line is the measured external quantum efficiency, and the dashed line is the external quantum efficiency simulated using COMSOL multiphysics. The navy dashed line is the simulated external quantum efficiency of a detector with the same absorber thickness, but no plasmonic layer or Au 2D metal grating. (c) Scanning electron micrograph of a fabricated PIQUE detector and an expanded view of the 2D metal grating.

with a peak EQE at $\lambda_0 = 10.4$ μm of ∼39%, a factor of 13.5× enhancement in response when compared to the same detector structure's absorption, simulated without the underlying plasmonic material or 2D metal grating, identical to the simulated absorption plotted in Fig. 2(a). The measured spectral response of the fabricated detector mirrors the absorption feature in Fig. 3(a), with the slight spectral shift coming from the difference in sample temperature between the two experiments. Notably, for the same T2SL material, we calculate that a detector with absorber thickness of $t \sim 7.5$ μm would be required to achieve the same EQE at $\lambda_0 = 10.4$ μm, optimistically assuming perfect photo-excited charge carrier collection efficiency in the thicker detector.

C. Temperature-Dependent Responsivity and Dark Current–Voltage

The ability to detect LWIR light, in a $\sim\lambda_0/33$-thickness detector, with effectively the same EQE as a wavelength-scale-thickness detector, has significant implications for our detector performance metrics given the relationship between D^* and detector thickness from Eq. (1). Figure 4(a) shows the measured detector dark current (solid lines) for temperatures from 78 K to 195 K, compared to the dark current for a HgCdTe detector at the same temperatures (dashes), the latter calculated from the Rule 07 heuristic [33], which provides a rule-of-thumb estimate for state-of-the-art IR detectors. To accurately compare our fabricated detector dark current, at each temperature, to the Rule 07 dark current, the appropriate operational bias of the plasmonic detectors must be determined. Figure 4(b) shows the temperature-dependent detector responsivity (at $\lambda_0 = 9.46$ μm) as a function of applied bias, with the strong saturation at low applied biases characteristic of nBn detectors and essential for compatibility with focal-plane-array (FPA) readout circuitry. We choose, for each temperature, an operational bias corresponding to peak specific detectivity. The

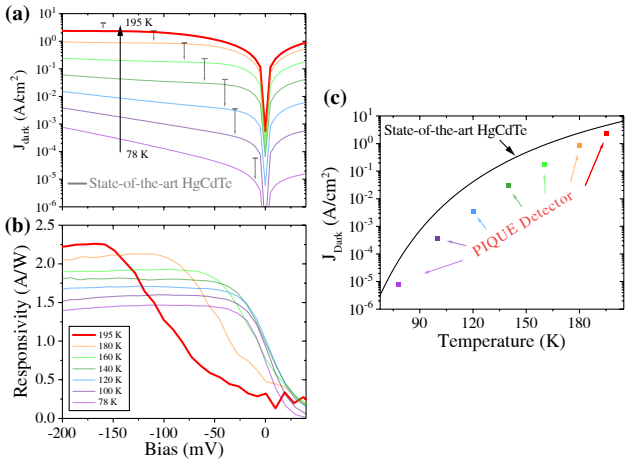

Fig. 4. (a) Dark current, as a function of applied bias, of the ultra-thin detector for temperatures between 78−195 K. The dash above each line is the commensurate Rule 07 dark current for each temperature, positioned at the bias of peak specific detectivity of the PIQUE detector. (b) Bias-dependent responsivity of the ultra-thin detectors taken at $\lambda_0 = 9.46$ μm as a function of temperature. As expected for a nBn detector, responsivity saturates at low voltages (−80 mV at $T = 78$ K and −160 mV at $T = 195$ K) and remains constant with increasing bias. A slight increase in detector responsivity is observed with increasing temperature, resulting from the redshifting of the T2SL bandgap. (c) PIQUE detector dark current as a function of temperature plotted with the Rule 07 heuristic for a detector with $\lambda_{co} = 11.42$ μm. We choose the comparison detector cutoff wavelength to be at 50% of the PIQUE's peak EQE (potentially significantly underestimating the actual Rule 07 dark current). As can be seen, from 78 K to 195 K the plasmonic detector dark current out performs an ideal MCT detector (while maintaining comparable EQE).

dark currents for these applied biases, as a function of temperature, are plotted in Fig. 4(c), along with the Rule 07 dark current (which is typically already an order of magnitude less than the dark current of a traditional, wavelength-scale, T2SL nBn detector [36–38]). Figure 4(c) clearly demonstrates that the PIQUE detector dark current, for the full temperature range (78–195 K) is substantially lower than the dark current for state-of-the-art MCT LWIR detectors. Specifically, our dark current is lowest, relative to Rule 07, at 110 K with a dark current 12.8 × lower than Rule 07. However, at elevated temperatures ($T = 195$ K), we observe dark currents only 1.94 × lower than Rule 07. We attribute our detector's dark current converging towards Rule 07 at elevated temperatures to the conservative choice of cutoff wavelength we use for the Rule 07 heuristic (choosing the wavelength where we observe 50% of maximum EQE). In reality, our detector's T2SL absorber cutoff wavelength has a strong temperature dependence, whereas the optical enhancement associated with the SPP is largely temperature independent. Thus, we expect if we used the bandgap of the T2SL for our Rule 07 curve, rather than 50% max EQE, we would maintain dark currents at least an order of magnitude lower than Rule 07 across the entire temperature range shown.

D. Detector Performance

The significantly reduced dark currents achievable in PIQUE detectors has a dramatic impact on the detectors' D^*. Figure 5 plots detector performance (D^*) as a function of wavelength for our PIQUE detectors, as well as state-of-the-art commercially available LWIR detectors. Shot- and Johnson-noise-limited

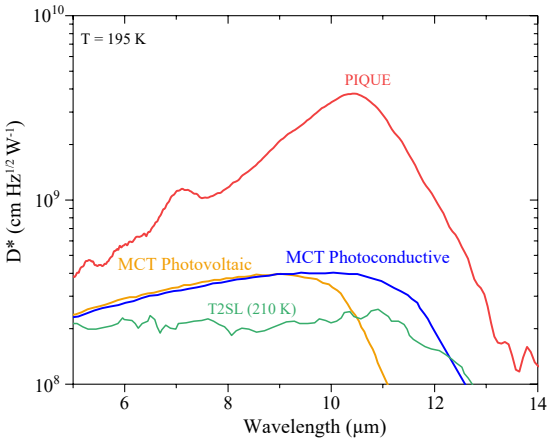

Fig. 5. (a) Spectral specific detectivity of the PIQUE detector and commercial LWIR detectors at comparable temperatures. As can be clearly seen, PIQUE detectors at 195 K substantially outperform commercial HgCdTe at 195 K and T2SL detectors at 210 K.

specific detectivity is estimated, using the measured responsivity and dark current, with the D^* expression provided in Supplement 1. As can be observed from this plot, the PIQUE detector substantially outperforms existing LWIR detectors, due to the significant improvement in dark current associated with the $\sim\lambda_0/33$ absorber thickness. This improvement in dark current can be realized without any degradation in EQE, a result of the strong field enhancement achieved in the plasmonic structure. The PIQUE detector exhibits peak $D^* \approx 4 \times 10^9$ cm Hz$^{1/2}$W^{-1} at $T = 195$ K, where the PIQUE detector outperforms both commercial T2SL [35] and MCT [34] detectors. However, the PIQUE detectors presented here are single-element, front-side illuminated (as are the comparison commercial detectors), and not well suited for the substrate-side-illumination required for most FPA designs. Future detector designs will look to reverse the order of growth (nBn detector, then n^{++} plasmonic layer) to enable coupling to SPPs from substrate-side illumination and thus FPA configurations.

The single greatest challenge for LWIR detectors is the demonstration of high performance at elevated temperatures. The detector performance of any LWIR photodetector degrades dramatically with increasing temperature, with D^* typically decreasing by two or more orders of magnitude as operating temperature increases from liquid nitrogen (77 K) to room (∼300 K) temperature. This degradation is almost completely a result of the exponential increase in dark current density, entirely expected for a semiconductor device whose effective bandgap energy is essentially the energy of the peak blackbody emission at detector operating temperatures near 300 K. Decreasing the dark current of a LWIR detector, for a given material system and detector design, can be achieved only by drastically reducing the detector volume, which for traditional detector architectures incurs a severe responsivity penalty. Not only do our PIQUE detectors provide a ∼20× reduction in absorber thickness (compared to state-of-the-art LWIR detectors), but they achieve this reduction in absorber thickness without any appreciable degradation of detector responsivity. These results and the presented PIQUE detector architecture offer a realistic path towards high-performance room-temperature LWIR detectors, in many ways the grail of LWIR detector work. Additionally, the monolithic integration of the LWIR PIQUE

detectors offers a unique and novel opportunity to explore all-epitaxial plasmonic optoelectronic device architectures while simultaneously realizing significant performance enhancement over existing mid-IR technologies.

4. CONCLUSION

In summary, we demonstrate a LWIR photodetector, leveraging a quantum-engineered T2SL absorber integrated into an nBn photodetector architecture, and embedded in a resonant epitaxial plasmonic structure. The strong confinement of incident light achieved by coupling into SPP modes at the detector/highly doped semiconductor interface allows for an ultra-thin detector architecture without any loss of detector responsivity. Moreover, the presented architecture is extremely versatile and could be implemented in other material systems and/or extended to longer wavelengths. We show detector dark currents 1.9 × below the Rule 07 heuristic, and peak EQEs of 39% (which would require thicknesses of the order of >7.5 μm in a traditional detector architecture). The presented detectors show specific detectivity above that of state-of-the-art commercial LWIR photodetectors, both MCT and T2SL. The PIQUE detectors presented in this work utilize a plasmonic-optoelectronic device design, leveraging epitaxial plasmonic materials with state-of-the-art performance. Moreover, the PIQUE detectors demonstrate a scalable plasmonic architecture for real world applications, capable of outperforming commercial detectors and offering a viable alternative to current, environmentally problematic and widely used detector materials.

Funding. Lockheed Martin; National Science Foundation (NNCI-1542159); Defense Advanced Research Projects Agency (NASCENT, NLM program); Division of Materials Research (1720595); Division of Electrical, Communications and Cyber Systems (1926187).

Disclosures. The authors declare no conflicts of interest.

Data availability. Data underlying the results presented in this paper are not publicly available at this time, but may be obtained from the authors upon reasonable request. The room-temperature reflection RCWA modeling was performed using a MATLAB software package from V. A. Podolskiy's research group (see [39] for implementation). The numerical absorption modeling was performed using COMSOL Multiphysics software. The specific simulation files and/or data related to either of these software packages or the code that analyzes the experimentally measured data are available from the corresponding author upon reasonable request.

Supplemental document. See Supplement 1 for supporting content.

REFERENCES

1. S. A. Maier, P. G. Kik, H. A. Atwater, S. Meltzer, E. Harel, B. E. Koel, and A. A. G. Requicha, "Local detection of electromagnetic energy transport below the diffraction limit in metal nanoparticle plasmon waveguides," Nat. Mater. **2**, 229–232 (2003).
2. J. N. Anker, W. P. Hall, O. Lyandres, N. C. Shah, J. Zhao, and R. P. Van Duyne, "Biosensing with plasmonic nanosensors," Nat. Mater. **7**, 442–453 (2008).
3. H. A. Atwater and A. Polman, "Plasmonics for improved photovoltaic devices," Nat. Mater. **9**, 205–213 (2010).
4. J. A. Schuller, E. S. Barnard, W. Cai, Y. C. Jun, J. S. White, and M. L. Brongersma, "Plasmonics for extreme light concentration and manipulation," Nat. Mater. **9**, 193–204 (2010).
5. M. A. Noginov, G. Zhu, A. M. Belgrave, R. Bakker, V. M. Shalaev, E. E. Narimanov, S. Stout, E. Herz, T. Suteewong, and U. Wiesner, "Demonstration of a spaser-based nanolaser," Nature **460**, 1110–1112 (2009).
6. R. F. Oulton, V. J. Sorger, T. Zentgraf, R. M. Ma, C. Gladden, L. Dai, G. Bartal, and X. Zhang, "Plasmon lasers at deep subwavelength scale," Nature **461**, 629–632 (2009).
7. M. T. Hill, M. Marell, E. S. P. Leong, B. Smalbrugge, Y. Zhu, M. Sun, P. J. van Veldhoven, E. J. Geluk, F. Karouta, Y.-S. Oei, R. Nötzel, C.-Z. Ning, and M. K. Smit, "Lasing in metal-insulator-metal sub-wavelength plasmonic waveguides," Opt. Express **17**, 11107–11112 (2009).
8. K. Nakayama, K. Tanabe, and H. A. Atwater, "Plasmonic nanoparticle enhanced light absorption in GaAs solar cells," Appl. Phys. Lett. **93**, 121904 (2008).
9. T. Nikolajsen, K. Leosson, and S. I. Bozhevolnyi, "Surface plasmon polariton based modulators and switches operating at telecom wavelengths," Appl. Phys. Lett. **85**, 5833 (2004).
10. J. B. Khurgin, "How to deal with the loss in plasmonics and metamaterials," Nat. Nanotechnol. **10**, 2–6 (2015).
11. K. Kneipp, Y. Wang, H. Kneipp, L. T. Perelman, I. Itzkan, R. R. Dasari, and M. S. Feld, "Single molecule detection using surface-enhanced Raman scattering (SERS)," Phys. Rev. Lett. **78**, 1667–1670 (1997).
12. S. Nie and S. R. Emory, "Probing single molecules and single nanoparticles by surface-enhanced Raman scattering," Science **275**, 1102–1106 (1997).
13. N. J. Hogan, A. S. Urban, C. Ayala-Orozco, A. Pimpinelli, P. Nordlander, and N. J. Halas, "Nanoparticles heat through light localization," Nano Lett. **14**, 4640–4645 (2014).
14. C. Loo, A. Lowery, N. Halas, J. West, and R. Drezek, "Immunotargeted nanoshells for integrated cancer imaging and therapy," Nano Lett. **5**, 709–711 (2005).
15. K. Okamoto, I. Niki, A. Shvartser, Y. Narukawa, T. Mukai, and A. Scherer, "Surface-plasmon-enhanced light emitters based on InGaN quantum wells," Nat. Mater. **3**, 601–605 (2004).
16. M.-K. Kwon, J.-Y. Kim, B.-H. Kim, I.-K. Park, C.-Y. Cho, C. C. Byeon, and S.-J. Park, "Surface-plasmon-enhanced light-emitting diodes," Adv. Mater. **20**, 1253–1257 (2008).
17. R. Stanley, "Plasmonics in the mid-infrared," Nat. Photonics **6**, 409–411 (2012).
18. S. Law, V. Podolskiy, and D. Wasserman, "Towards nano-scale photonics with micro-scale photons: the opportunities and challenges of mid-infrared plasmonics," Nanophotonics **2**, 103–130 (2013).
19. S. Law, D. C. Adams, A. M. Taylor, and D. Wasserman, "Mid-infrared designer metals," Opt. Express **20**, 12155–12165 (2012).
20. A. J. Hoffman, L. Alekseyev, S. S. Howard, K. J. Franz, D. Wasserman, V. A. Podolskiy, E. E. Narimanov, D. L. Sivco, and C. Gmachl, "Negative refraction in semiconductor metamaterials," Nat. Mater. **6**, 946–950 (2007).
21. L. Nordin, K. Li, A. Briggs, E. Simmons, S. R. Bank, V. A. Podolskiy, and D. Wasserman, "Enhanced emission from ultra-thin long wavelength infrared superlattices on epitaxial plasmonic materials," Appl. Phys. Lett. **116**, 021102 (2020).
22. L. Nordin, A. Kamboj, P. Petluru, E. Shaner, and D. Wasserman, "All-epitaxial integration of long-wavelength infrared plasmonic materials and detectors for enhanced responsivity," ACS Photon. **7**, 1950–1956 (2020).
23. C. H. Grein, P. M. Young, and H. Ehrenreich, "Minority carrier lifetimes in ideal InGaSb/InAs superlattices," Appl. Phys. Lett. **61**, 2905–2907 (1992).
24. S. Maimon and G. W. Wicks, "nBn detector, an infrared detector with reduced dark current and higher operating temperature," Appl. Phys. Lett. **89**, 151109 (2006).
25. D. Z. Y. Ting, C. J. Hill, A. Soibel, S. A. Keo, J. M. Mumolo, J. Nguyen, and S. D. Gunapala, "A high-performance long wavelength superlattice complementary barrier infrared detector," Appl. Phys. Lett. **95**, 23508 (2009).
26. A. Rogalski, *Infrared Detectors*, 2nd ed. (CRC Press, 2010).
27. D. Lee, P. Dreiske, J. Ellsworth, R. Cottier, A. Chen, S. Tallaricao, A. Yulius, M. Carmody, E. Piquette, M. Zandian, and S. Douglas, "Law 19: the ultimate photodiode performance metric," Proc. SPIE **11407**, 114070X (2020).
28. European Union, "Directive 2011/65/EU of The European Parliament and of the Council of 8 June 2011 on the restriction of the use of certain hazardous substances in electrical and electronic equipment," Off. J. EU **L174**, 88–100 (2011).
29. D. Palaferri, Y. Todorov, A. Bigioli, A. Mottaghizadeh, D. Gacemi, A. Calabrese, A. Vasanelli, L. Li, A. G. Davies, E. H. Linfield, F. Kapsalidis, M. Beck, J. Faist, and C. Sirtori, "Room-temperature nine-μm-wavelength photodetectors and GHz-frequency heterodyne receivers," Nature **556**, 85–88 (2018).

30. J. C. Campbell and A. Madhukar, "Quantum-dot infrared photodetectors," Proc. IEEE **95**, 1815 (2007).
31. A. V. Barve, T. Rotter, Y. Sharma, S. J. Lee, S. K. Noh, and S. Krishna, "Systematic study of different transitions in high operating temperature quantum dots in a well photodetectors," Appl. Phys. Lett. **97**, 061105 (2010).
32. X. Lu, J. Vaillancourt, and M. J. Meisner, "Temperature-dependent photoresponsivity and high-temperature (190 K) operation of a quantum dot infrared photodetector," Appl. Phys. Lett. **91**, 051115 (2007).
33. W. E. Tennant, D. Lee, M. Zandian, E. Piquette, and M. Carmody, "MBE HgCdTe technology: a very general solution to IR detection, described by "rule 07", a very convenient heuristic," J. Electron. Mater. **37**, 1406–1410 (2008).
34. Vigo System, "PCI-4TE series HgCdTe detectors datasheet," 2021, https://vigo.com.pl/wp-content/uploads/2021/04/PCI-4TE-series-datasheet-1.pdf.
35. Vigo System, "PCAS-3TE-12-0.1×0.1-to8-wznsear-70 datasheet," 2021, https://vigo.com.pl/wp-content/uploads/2021/05/PCAS-3TE-12-0.1x0.1-TO8-wZnSeAR-70-ENGINEERING-SAMPLE.pdf.
36. A. Rogalski, P. Martyniuk, and M. Kopytko, "Type-II superlattice photodetectors versus HgCdTe photodiodes," Prog. Quantum Electron. **68**, 100228 (2019).
37. D. R. Rhiger, "Performance comparison of long-wavelength infrared type II superlattice devices with HgCdTe," J. Electron. Mater. **40**, 1815–1822 (2011).
38. A. Rogalski, P. Martyniuk, and M. Kopytko, "InAs/GaSb type-II superlattice infrared detectors: future prospect," Appl. Phys. Rev. **4**, 031304 (2017).
39. V. A. Podolskiy, "Rigorous coupled wave analysis (RCWA) codes," MATLAB (2020), http://faculty.uml.edu/vpodolskiy/codes/index.html